ACS APPLIED MATERIALS & INTERFACES

Research Article

www.acsami.org

Microstructure Tailoring of the Nickel Oxide–Yttria-Stabilized Zirconia Hollow Fibers toward High-Performance Microtubular Solid Oxide Fuel Cells

Tong Liu,[†] Cong Ren,[†] Shumin Fang, Yao Wang, and Fanglin Chen*

Department of Mechanical Engineering, University of South Carolina, Columbia, South Carolina 29208, United States

ABSTRACT: NiO–yttria-stabilized zirconia (YSZ) hollow fiber anode support with different microstructures was prepared using a phase-inversion method. The effect of the solid loading of the phase-inversion suspensions on the microstructure development of the NiO-YSZ anode support was investigated. Solid loading in the suspension was found to have an important influence on the microstructure of the NiO-YSZ anode support and viscosity-related viscous fingering mechanism can be adopted to explain the pore formation mechanism of the as-prepared hollow fibers. NiO-YSZ anode-supported microtubular solid oxide fuel cells (SOFCs) with different anode microstructures were fabricated and tested, and the correlation between the anode support microstructures, porosity, gas permeability, electrical conductivity, and the cell electrochemical performance was discussed. Microtubular SOFCs with a cell configuration of Ni-YSZ/YSZ/YSZ-LSM (LSM = $(La_{0.8}Sr_{0.2})_{0.95}MnO_{3-x}$) and optimized anode microstructure show cell output power density of 833.9 mW cm^{-2} at 750 °C using humidified H_2 as fuel and ambient air as oxidant.

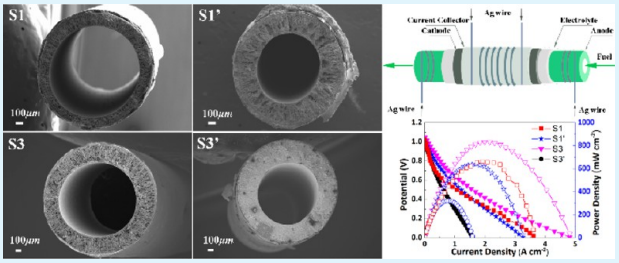

KEYWORDS: *microtubular SOFC, phase inversion, solid loading, viscosity, viscous fingering*

1. INTRODUCTION

Solid oxide fuel cells (SOFCs) have received considerable attention as potential future energy conversion technology for stationary and portable applications due to their unique advantages such as high conversion efficiencies, low emissions, fuel flexibility, and high tolerance to fuel impurities.[1−3] Planar and tubular SOFCs are currently two major geometric configurations.[2] Tubular SOFCs enable the design of SOFC stacks with high volumetric power density by reducing tube diameter.[4,5] Furthermore, tubular SOFCs have demonstrated robustness for repeated thermal cycling, even under rapid temperature gradients up to 4000 °C/min.[2,6] In particular, microtubular SOFCs (MT-SOFCs) with small tube diameter have recently attracted great attention due to their lower operating temperature, greater tolerance to thermal cycling, quicker start-up capability, higher volumetric power density, and lower overall materials cost by reducing cell weight compared with the conventional tubular SOFCs.[4,5] According to the different cell configuration, anode-,[7−13] electrolyte-,[14−16] and cathode[17−19]-supported MT-SOFCs have been explored. Among them, anode-supported MT-SOFCs having a thick anode layer as the cell structural support have been shown to be the most promising due to the excellent cell performance, sufficient mechanical strength, and less challenge for sealing and manifolding.[2,7−11] However, this design, undoubtedly, leads to a large resistance to the diffusion of gaseous fuel and products in the anode during operation. To decrease the mass transport resistance and improve the electrochemical performance, an immersion-induced phase-inversion technique has been developed to fabricate hollow fiber anode support with a thin spongelike layer and a thick fingerlike layer serving as anode functional layer and gas transport channels, respectively.[8−12,20] Since it was first reported by Loeb and Sourirajan in the early 1960s,[21] the phase-inversion method has been widely used as a unique technique to prepare asymmetric membranes for seawater treatment,[21−23] gas separation,[24−29] MT-SOFCs,[8−11,13,20] and other separation processes.[30,31] In these studies, the as-obtained hollow fiber membrane typically possesses two types of microstructures, a thick porous layer of large fingerlike macrovoids and a thin porous layer of small spongelike pores. To better control the microstructure of the hollow fiber anode support prepared by the phase-inversion method for MT-SOFCs, it is critical to understand the mechanism of the phase-inversion process. Although it has been generally accepted that the phase inversion of polymer solutions occurs according to the nucleation and growth mechanism and that the formation of fingerlike macrovoids is caused by diffusional flows of solvent from the polymer solution surrounding the nuclei,[32−34] recently, a new mechanism has been proposed that fingerlike macrovoids in ceramics may be induced by viscous fingering.[35−38] Both mechanisms have been supported by experimental evidence, and further studies are critically needed to clarify conditions where one mechanism

Received: July 17, 2014
Accepted: October 14, 2014
Published: October 14, 2014

may prevail to better design the microstructure of the hollow fiber.

It has been reported that the viscosities of the phase-inversion suspensions could be controlled by introducing nonsolvent additives such as H_2O and ethanol into the casting slurries,[35−38] where the formation of the fingerlike macrovoids in the hollow fiber was suppressed and the thickness of this structure was reduced since H_2O and ethanol are poor solvents but good dispersing agents. Accordingly the microstructure of the hollow fiber is expected to be significantly influenced by the initial viscosity in the phase-inversion suspension.[35−38] The objective of this study is to evaluate how viscosity of the phase-inversion suspension influences the microstructures of the hollow fibers by changing the solid loading in the phase-inversion suspensions.

In this work, NiO-YSZ anode supports prepared from the phase-inversion suspensions with different solid loading were successfully prepared. The pore formation mechanism was evaluated using the viscous fingering mechanism, and the effects of processing parameters on the microstructure development evolution were systematically investigated. Furthermore, microtubular NiO-YSZ anode-supported SOFCs with four different unique anode microstructures were fabricated, and their corresponding performance and properties were evaluated.

2. EXPERIMENTAL

2.1. Materials. Commercial NiO (JT Baker, USA) and YSZ (TZ-8Y, Tosoh Corporation, Tokyo, Japan) anode powders were mixed in a weight ratio of 6:4 by planetary ball milling in ethanol for 2 h and then dried at 80 °C overnight. Polyethersulfone (PESf) (Veradel 3000P, Solvay Specialty Polymers, USA) with a molecular weight of ∼3000 g mol^{-1}, *N*-methyl-2-pyrrolidone (NMP) (HPLC grade, Sigma-Aldrich, USA), and polyvinylpyrrolidone (PVP) (K30, CP, Sinopharm Chemical Reagent Co., China) with a molecular weight of 45 000−55 000 g mol^{-1} were used as the polymer binder, the solvent, and dispersant, respectively, to prepare the organic solution. Deionized water was used as the internal and external coagulants for preparation of hollow fibers, and all preparation processes were done at room temperature.

2.2. Preparation and Characterization of NiO−YSZ Support. The phase-inversion method was applied to fabricate the NiO-YSZ hollow fibers.[8−12] In the preparation process, PVP and PESf were dissolved in NMP solution prior to the addition of NiO-YSZ composite powders with different solid loading. The parameters of the suspension were given in Table 1. These mixtures were ball-milled for 48 h. Before the preparation of hollow fibers, the suspensions were degassed under vacuum at room temperature until no bubbles were observable. For the extrusion method, a schematic diagram of which was shown in Figure 1A, the as-prepared NiO-YSZ suspensions were extruded through a tube-in-orifice spinneret (outer diameter 2.6 mm, inner diameter 1.0 mm) using pressurized nitrogen (0.2 bar). Deionized water was pumped through the bore of the spinneret at a speed of 10 mL min^{-1} exactly controlled by a nitrogen-induced flow using a digital mass flow controller (Alicat Scientific Inc., USA). After passing an air gap of 10 mm, the fibers were immersed in a water bath for further solvent exchange to take place. For the coating method, a schematic diagram of which was shown in Figure 1B, the glass rod with a diameter of 1.6 mm was immersed into the as-prepared NiO-YSZ suspension for 2 min and then taken out, followed by immediate immersion into a water bath for 24 h to complete the solvent exchange. All as-prepared fibers were then dried at room temperature in open air for a week, heated at a rate of 1 °C/min to 600 °C and maintained at that temperature for 2 h to remove the organic polymer binder, and then heated to 1200 °C with 2 h of dwell time in air to achieve sufficient mechanical strength for subsequent coating YSZ film electrolyte.

Table 1. Suspension Composition for Preparation of Ni-YSZ Hollow Fibers

composite	weight (g)	solid loading (%)	specimen number[a]
NMP	18		
PESf	3		
PVP (K30)	0.75		
NiO-YSZ	45.0	67.4	S1, S1′
(m_{NiO}/m_{YSZ} = 6:4)	56.2	72.1	
	67.5	75.6	S2, S2′
	75	77.5	
	90	80.5	S3, S3′

[a]Hollow fiber S1−3: the extrusion method, S1′−3′: the coating method.

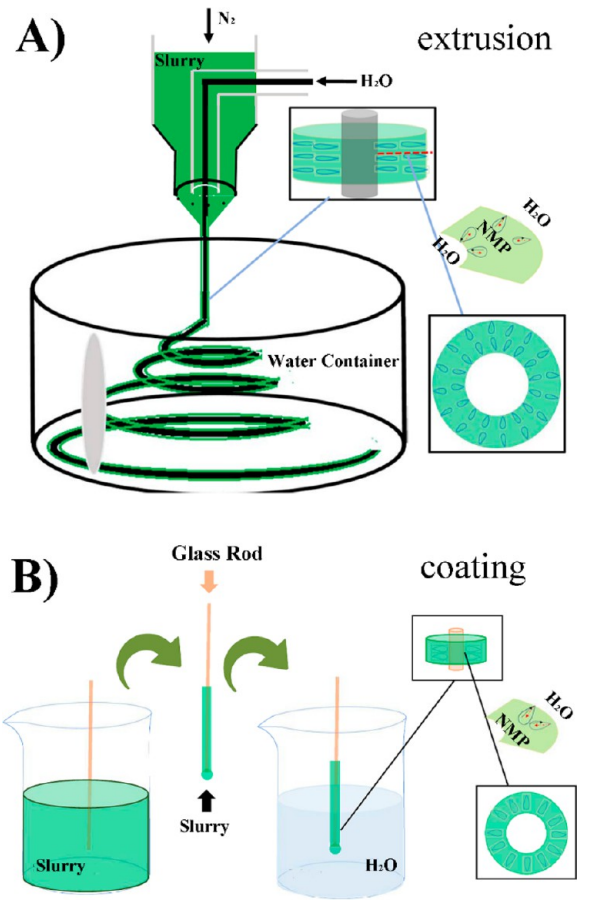

Figure 1. Schematic diagram of the setup for preparation of NiO-YSZ hollow fiber anode support. (A) The extrusion method. (B) The coating method.

Rheological properties of suspensions were determined using an AR Rheometer (Model AR2000 ex, TA Instrument Co., USA) at 25 °C. After the suspensions were presheared for 30 s, the measurements were performed by stepping up to high shearing rates. The morphologies of the hollow fibers were studied using scanning electron microscopy (SEM, Zeiss Ultra Plus FESEM, Germany).

To test the gas permeability, electrical conductivity, and porosity of the as-obtained Ni-YSZ anode support, the hollow fibers were first sintered at 1450 °C for 5 h in air and then reduced at 800 °C for 5 h in humidified H_2. The gas permeability was then measured.[39] The electrical conductivity was measured at room temperature using a

Keithley 2001 Multimeter via the four-probe method. The porosity was determined using the Archimedes method in water.

2.3. Preparation and Performance Measurement of MT-SOFCs. Thin YSZ electrolyte membrane was coated on the prefired NiO-YSZ hollow fiber anode support by a dip-coating method and cosintered at 1450 °C for 5 h with a heating and cooling rate of 2 °C/min.[8−12] YSZ and $(La_{0.8}Sr_{0.2})_{0.95}MnO_{3-x}$ (LSM80-HP, Fuel Cell Materials, USA) powders at weight ratio of 50:50 were ground with terpilenol to form a cathode ink, which was then printed onto the YSZ electrolyte film by a brush painting method, followed by firing at 1100 °C for 2 h. The active cathode area was 0.3 cm^2.

A silver grid was printed on the surface of the cathode to collect the cathodic current, and Ag wire was used as the current lead, while the Ag wires were directly attached to the two ends of the microtubular SOFCs to collect the anodic current. SOFC performance evaluation was carried out in a single-cell testing setup, as schematically shown in Figure 2. The anode was exposed to humidified H_2 (3 vol % H_2O)

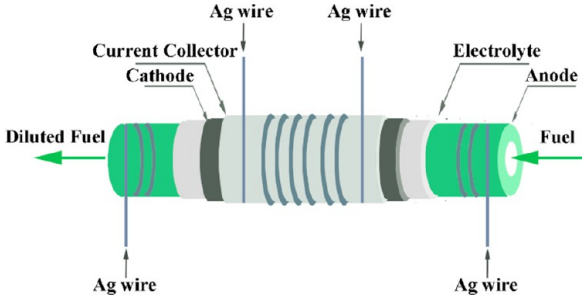

Figure 2. Schematic diagram of the setup for electrochemical performance measurement of microtubular SOFCs.

atmosphere with H_2 flow rate of 40 mL/min, while the cathode was exposed to ambient air. The current−voltage (I−V) curves and electrochemical impedance spectra (EIS) were performed using a VersaStudio electrochemistry analyzer. For EIS measurement, the frequency range was from 1 MHz to 0.01 Hz, and the AC amplitude was 10 mV.

3. RESULTS AND DISCUSSION

3.1. Rheological Behavior of NiO-YSZ Suspensions. Figure 3 shows the relationship between the viscosity of the suspension and the solid loading. Figure 3A shows the influence of the shearing rate on the viscosity. At any given solid loading, the viscosity of the NiO-YSZ suspension decreases with increasing the shearing rate from 0.01 to 100 s^{-1}. At any given shearing rate, the viscosity of the suspension increases with increasing the solid loading in the suspension. Note from Figure 3B that for the suspension with low solid loading, with increase in the solid loading, the suspension viscosity value increases very slowly. When the solid loading reaches a critical value, further increase in the solid loading will result in a sharp viscosity increase. It has been reported that the viscosity has significant effects on the morphology and is a dominating factor for preparation of hollow fibers.[35−38] Thus, in this study, to investigate the viscosity or solid loading effect on the microstructures/morphologies, the suspension with the solid loading of 67.4, 75.6, and 80.5 wt % were chosen to fabricate a series of NiO-YSZ hollow-fiber anode supports. For simplification, the hollow-fiber membranes prepared by adjusting the solid loading were marked as S1, S2, S3 (prepared from the extrusion method) and S1′, S2′, S3′ (prepared from the coating method).

3.2. Effects of the Solid Loading on the Microstructure. During the preparation of the series of the S1−S3

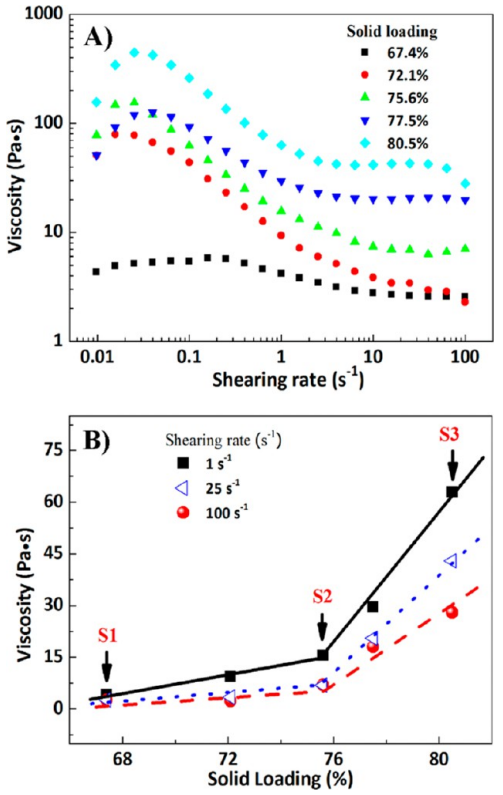

Figure 3. Rheological properties of the suspensions derived from different solid loading. (A) Viscosity vs shearing rate. (B) Viscosity vs solid loading.

hollow fibers, except the solid loading for the spinning hollow fiber precursors, all other processing parameters were fixed at the same conditions. Therefore, the change of the morphology and other membrane properties is mainly attributed to the variation of the solid loading. Figure 4 shows the cross-sectional

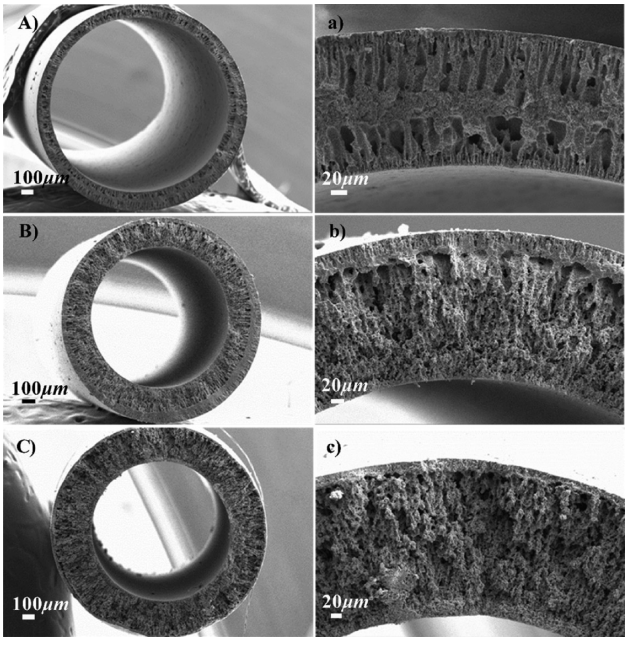

Figure 4. Cross-sectional SEM images of the as-obtained hollow fibers prepared using the extrusion method. (A-a) S1, (B-b) S2, (C-c) S3.

dx.doi.org/10.1021/am5046907 | ACS Appl. Mater. Interfaces 2014, 6, 18853−18860

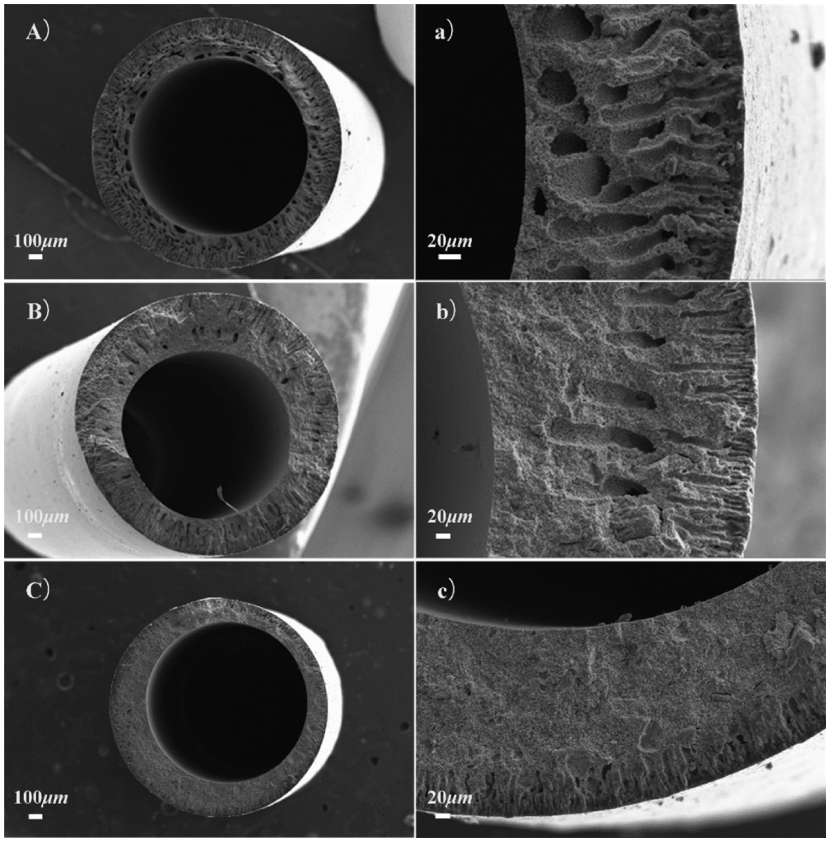

Figure 5. Cross-sectional SEM images of the as-obtained hollow fibers prepared using the coating method. (A-a) S1′, (B-b) S2′, (C-c) S3′.

SEM images of the hollow fibers prefired at 1200 °C for 2 h prepared from the extrusion method. It can be seen that spongelike pores and fingerlike voids are simultaneously present in the hollow fibers, forming an asymmetric morphology of the hollow fibers. The S1 hollow fibers derived from the low solid loading exhibit a sandwich structure, that is, a central spongelike layer between two fingerlike macrovoid layers, as shown in Figure 4A-a, and the thickness of the fingerlike structure near the inner surface and outer surface is similar, approximately 35% of the fiber thickness. When the solid loading increases to a critical point (S2), the fingerlike structure near the outer surface gradually diminishes, while the fingerlike macrovoids layer near the inner surface gradually extends to the outer surface and the central spongelike layer moves outward, as shown in Figure 4B-b. Further increasing the solid loading in the suspension (S3), the fingerlike macrovoids layer near the outer surface almost disappears and the fingerlike macrovoids layer from the inner surface almost straightly extends to the outer surface, leaving only one thin spongelike layer on the outer surface of the hollow fibers supported on a thick fingerlike layer, as shown in Figure 4C-c.

From Figure 4 it can be seen that the different viscosity of the phase-inversion suspension has an important influence on the hollow fiber morphology evolution process, but is different from what has been reported,[36,37] possibly due to the different morphology formation mechanisms. To investigate the solid loading effect on the pore formation mechanism, a coating method as schematically shown in Figure 1B was also used to fabricate the NiO-YSZ hollow fibers. In the coating approach, external exchange between NMP and H_2O was almost the same as that of the extrusion method, but internal exchange between NMP and H_2O was prohibited, resulting in different microstructure of the hollow fibers. Figure 5 shows the cross-sectional SEM images of the hollow fibers prepared using the coating method and prefired at 1200 °C for 2 h. It can be seen that spongelike pores and fingerlike macrovoids are also simultaneously present in the hollow fibers, forming asymmetric morphologies of the hollow fibers. With low solid loading, the fingerlike macrovoids in the S1′ hollow fibers are supported on a thin spongelike layer near the inner surface and almost penetrate through the entire fiber thickness, as shown in Figure 5A-a. When the solid loading increases to a critical point (S2′), the thickness of the spongelike layer near the inner surface gradually increases, while the thickness of the fingerlike macrovoid layer near the outer surface gradually decreases, as shown in Figure 5B-b. Further increasing the solid loading in the suspension, the fingerlike macrovoid layer near the outer surface of S3′ hollow fibers almost disappears, and hollow fiber with predominantly spongelike structure is obtained, as shown in Figure 5C-c.

From Figures 4 and 5, it can be seen that the microstructure of the NiO-YSZ hollow fibers can be controlled by adjusting the solid loading (viscosity) in the initial suspension and the preparation method (the extrusion or coating method) during the phase-inversion process. For other material systems, before the preparation of the hollow fiber, the rheological properties of the phase-inversion suspension with different solid loading should be studied, and then the hollow fiber with desired microstructure for specific application can be prepared by selecting the suitable phase-inversion suspension and preparation method. For example, for the suspension with low solid loading, the extrusion method can be used to prepare sandwichlike hollow fibers, but the coating method can be used to prepare hollow fiber with predominately fingerlike

layer. However, for suspension with high solid loading, the extrusion method can be used to prepare the hollow fiber with thin spongelike layer supported on long-fingerlike layer, but the coating method can be used to prepare hollow fiber with predominately spongelike layer.

3.3. Pore Formation Mechanism. In this work, NiO-YSZ powders with different weights were added into the NMP/PESf/powders system as a viscosity modifier. Comparing Figures 4 and 5, it can be seen that the microstructures of the hollow fibers were significantly modified by adjusting the viscosities of the phase-inversion suspensions, indicating that there is strong correlation between viscosity and viscous fingering phenomenon. Therefore, the viscosity-related viscous fingering mechanism is adopted in this work to explain the pore formation mechanism/process. For the hollow fibers prepared using the extrusion method, a 10 mm thick air gap will result in a simultaneous solvent evaporation and moisture (nonsolvent H_2O) condensation, causing a local viscosity increase in the outer surface of the fiber prior to immersion. Consequently, a thin spongelike layer is formed (shown in Figure 4). During the time the nascent fiber is exposed to the atmosphere (10 mm thick air gap), the viscosity of the outer surface increases, which will inhibit the viscous fingering phenomena and the subsequent growth of the fingerlike voids at the outer surface, especially for the suspension with high solid loading, since increasing the solid loading will significantly increase the viscosity (Figure 3B), which will inhibit and even terminate the viscous fingering phenomena. Therefore, the fingerlike layer near the outer surface will gradually diminish, even disappear, which is in agreement with the morphology evolution of the hollow fibers prepared using the coating method (Figure 5), indicating that the pore formation evolution derived from the varied viscosity (solid loading) is controlled by the viscous fingering mechanism.[35−38]

Note that the fingerlike layer near the inner surface in Figure 4 will gradually extend to the outer surface with increasing the solid loading, implying that increasing the viscosity has no significant influence on the viscous fingering phenomena near the inner surface. The reason may be that as NMP in the nascent fiber will exchange with H_2O immediately, no blocking layer (spongelike layer) is formed; thus, the fingerlike layer will penetrate into the fiber cross-section directly, especially when the fingerlike layer near the outer surface is prevented at high solid loading, and less H_2O can be introduced into the fiber cross-section from the outer surface, leading to larger NMP and/or H_2O concentration gradient between inner surface and central wall. According to inverse relationship between interdiffusion coefficient and the viscosity of the suspension reported by Tyn and Calus,[40] the increased viscosity will decrease the interdiffusion coefficients between NMP and H_2O ($D_{H2O\text{-}NMP}$ and $D_{NMP\text{-}H2O}$) near the inner surface, but due to the larger NMP and/or H_2O concentration gradient between the inner surface and the central wall, an interesting phenomenon is observed, namely, that the viscous fingering phenomena can still be enhanced, and longer fingerlike macrovoids layer can be achieved, as shown in Figure 4C-c. At the same time, due to the increased solid loading in the suspension, the polymer/ceramic powder ratio decreases, and the polymer coverage of ceramic powder decreases. Consequently, the powders may aggregate, and the fingerlike macrovoids aggregation to larger fingerlike macrovoids will be hindered. Therefore, with the increase in the solid loading, the pore size will decrease, but the pore number (microchannel) will increase.

3.4. Gas Permeability and Electrical Conductivity of the NiO-YSZ Hollow Fibers. To study the microstructure effect on the gas permeability, porosity, electrical conductivity, and electrochemical performance of the NiO-YSZ anode support, four representative hollow fibers S1 (sandwich), S3 (asymmetric with functional layer), S1′ (asymmetric without functional layer), and S3′ (spongelike) were chosen to fabricate anode-supported MT-SOFCs.

To have high cell performance, the anode support should have sufficient porosity with low tortuosity facile mass transport in the anode.[41] Table 2 shows the porosity of the Ni-YSZ hollow fibers. It can be seen that the hollow fibers with fingerlike macrovoids exhibit higher porosity (>65.3%) than the hollow fiber S3′ with spongelike small pores (41.3%), especially for the hollow fiber S1 with sandwich structure, where the porosity can reach 68.2%. Higher porosity is beneficial to mass transport.

Table 2. Gas Permeability, Electrical Conductivity, and Porosity of the Ni-YSZ Hollow Fibers

	specimen number				
	S1	S1′	S3	S3′	order
permeability (10^4 L m^{-2} h^{-1} bar^{-1})	68.5	35.1	27.6	3.2	S1 > S1′ > S3 > S3′
$\sigma_{Ni\text{-}YSZ}$ (S cm^{-1})	195	192	197	276	S1 ≈ S1′ ≈ S3 < S3′
porosity (%)	68.2	65.3	66.0	41.3	S1 > S3 > S1′ ≫ S3′

To investigate the mass deliverability of the hollow fibers, the gas permeation analysis was used. Figure 6 shows the N_2 permeance and permeability of the Ni-YSZ hollow fibers that were obtained by sintering NiO-YSZ hollow fibers at 1450 °C for 5 h in air and then reducing at 800 °C for 5 h in the humidified H_2. It can be seen that the N_2 permeance and gas permeability through the Ni-YSZ hollow fibers highly depend on the microstructure, and fingerlike macrovoids layer in the hollow fiber presents higher gas permeability compared with spongelike layer (hollow fiber S1 > S3), indicating that the fingerlike macrovoids can serve as effective channels for facile mass deliverability, while the spongelike layer will restrict gas transport. However, the spongelike layer near the anode/

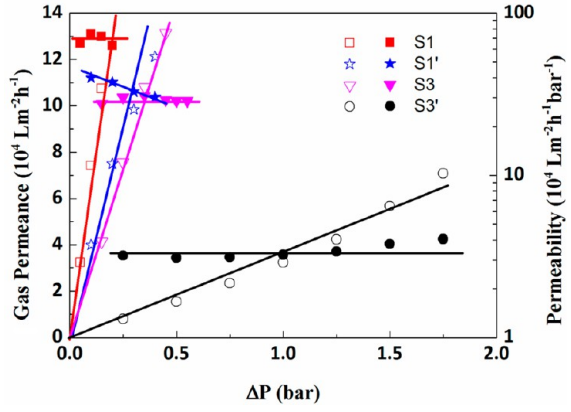

Figure 6. Gas permeability of the Ni-YSZ hollow fibers fired at 1450 °C for 5h in the air and then reduced at 800 °C for 5 h in the humidified H_2. The open symbols and the solid symbols denote gas permeance and gas permeability, respectively.

electrolyte interface can provide more surface area for the electrochemical reactions, consequently serving as anode functional layer and enhancing the electrochemical performance.

Ni-YSZ anode support is required to possess an appropriate electrical conductivity for current collection.[41] There are two phases in Ni/YSZ cermet, one is metallic Ni, which is an excellent electronic conductor, and the other is YSZ, which is a good oxygen ionic conductor. To obtain high electrical conductivity and catalytic activity, both Ni and YSZ phases must form their own continuous network and provide a large number of three phase boundaries (TPBs). The overall conductivity of the sample is dominated by the Ni phase since the conductivity of metallic Ni is 5 orders of magnitude higher than that of YSZ.[42] Table 2 shows the electrical conductivity of the Ni-YSZ hollow fibers. It can be noted that the hollow fiber S3′ with spongelike small pores possesses higher electrical conductivity (276 S cm^{-1}), while the hollow fibers with fingerlike macrovoids exhibit lower electrical conductivity (192−197 S cm^{-1}) but sufficient for current collection.

Ni-YSZ hollow fibers S1, S1′, and S3 exhibit considerable porosity (>65.3%), gas permeability (27.6∼68.5 × 10^4 L m^{-2} h^{-1} bar^{-1}), and electrical conductivity (192−197 S cm^{-1}), suitable for MT-SOFCs application. Meanwhile, the Ni-YSZ hollow fiber S3′ possesses excellent electrical conductivity (276 S cm^{-1}) but very low porosity (41.3%) and gas permeability (3.2 × 10^4 L m^{-2} h^{-1} bar^{-1}), and it may not be suitable for MT-SOFCs application.

3.5. Electrochemical Performance of Microtubular NiO-YSZ Supported SOFCs. To investigate the correlation between the microstructure and the electrochemical performance of the MT-SOFCs, four MT-SOFCs with the cell configuration of Ni-YSZ/YSZ/YSZ-LSM and different anode microstructures corresponding to the as-prepared hollow fibers S1, S3, S1′, and S3′ were fabricated and denoted as cell S1, cell S3, cell S1′, and cell S3′, respectively. Figure 7 shows cross-sectional SEM images of the as-obtained MT-SOFCs with different anode microstructures. The YSZ electrolyte film is fabricated using a dip-coating method in which YSZ particles are deposited on the outer surface of the anode substrate through capillary force. Consequently, anode morphology has an important impact on the thickness of the YSZ electrolyte film. Although the YSZ electrolyte film for all the cells was prepared with the same procedure, the thickness of the YSZ electrolyte was different, mainly due to the microstructural difference of the anode substrate. For cells S1, S3, S1′, and S3′, the thickness of the YSZ electrolyte film is 10, 8, 10, and 15 μm, respectively.

The electrochemical performances of the MT-SOFCs were evaluated by measuring the polarization characteristics of the cells at 750 °C with humidified H_2 as fuel and ambient air as oxidant. As shown in Figure 8A, for cells S1, S3, S1′, and S3′, the open-circuit voltages (OCV) are 1.02, 1.05, 1.02, and 1.01V, respectively. From the $I-P$ plots shown in Figure 8A, it can be seen that the cell maximum output power densities of 663.6, 833.9, 636.1, and 322 mW cm^{-2} are achieved at 750 °C for cells S1, S3, S1′, and S3′, respectively, and the optimal maximum output power density of 833.9 mW cm^{-2} is higher than or at least the same as the results previously reported at 750 °C,[8,9,43−45] indicating that the electrochemical performance of the MT-SOFCs can be significantly improved by tailoring the microstructure of the anode support. As for cell S3′, the anode

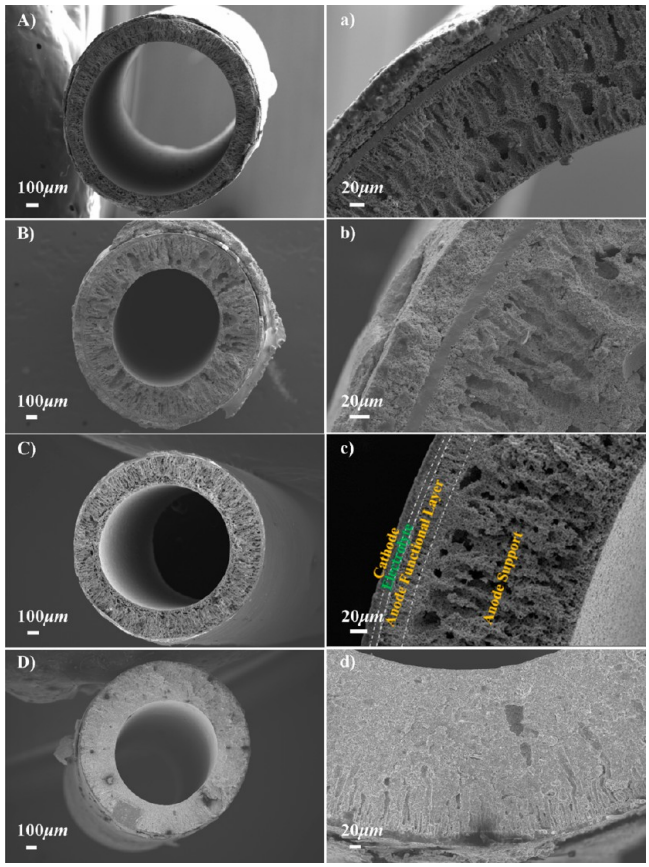

Figure 7. Cross-sectional SEM images of cells with different anode microstructures. (A-a) cell S1, (B-b) cell S1′, (C-c) cell S3, and (D-d) cell S3′.

support with predominately spongelike layer, possessing lower porosity, higher tortuosity, and lower gas permeability than the anode support with fingerlike macrovoids (Figure 7), significantly affects not only the YSZ electrolyte film thickness (15 μm thick) but also the H_2 diffusion and lowers its cell electrochemical performance, indicating that porosity and gas permeability of the anode support has an important effect on the fuel transportation and electrochemical performance; however, at the same time, the order of porosity (S1 ≈ S1′ ≈ S3) and gas permeability (S1 > S1′ > S3) does not agree with the order of electrochemical performance (S3 > S1 ≈ S1′), implying that the anode functional layer near the electrolyte/anode interface also plays a critical role in electrochemical performance.[41] For cell S3 (Figure 7C-c), an ∼30 μm thick nearly spongelike layer adjacent to electrolyte YSZ can serve as anode functional layer, providing a large number of TPBs and therefore promoting H_2 oxidation and enhancing the cell electrochemical performance; for cells S1 and S1′, fingerlike macrovoids layer near electrolyte/anode interface will reduce the electrolyte/anode connection and the amount of TPBs, thus lowering their electrochemical performance. Figure 8B,C displays electrochemical impedance spectra (EIS) of the four cells under OCV conditions at 750 °C. The high-frequency intercept represents the ohmic resistance (R_o) of the cells, while the low-frequency intercept corresponds to the total cell resistance (R_t), including ohmic resistance (R_o), and polarization resistance (R_p).[46] The overall size of the impedance arcs is attributed to the cell polarization resistance (R_p), including both activation polarization resistance and concentration

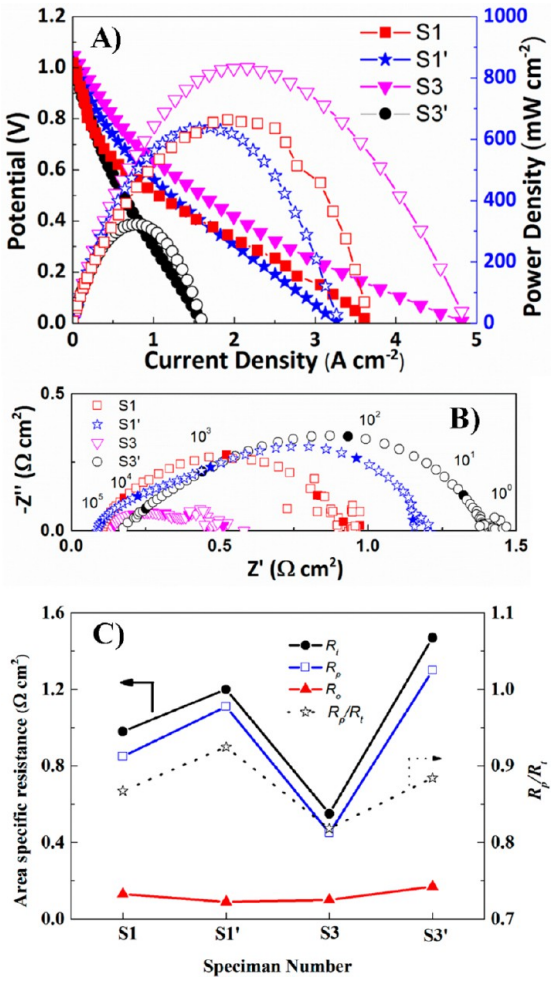

Figure 8. Performance of the Ni-YSZ/YSZ/YSZ-LSM microtubular cells at 750 °C with humidified H_2 as fuel and ambient air as oxidant. (A) Cell voltage and power density as a function of current density. (B) Impedance spectra of the cells measured under open-circuit conditions. (C) The total cell resistance (R_t), interfacial polarization resistance (R_p), ohmic resistance (R_o) as determined from the impedance spectra as shown in (B), and R_p/R_t.

polarization resistance. Since the cathode microstructure is similar and the cathode resistance (R_c) is expected to be similar, the difference in the electrode polarization resistances from the different cells will be mainly attributed to the anode microstructure. Therefore, the electrochemical performance of the MT-SOFCs can be significantly improved by tailoring the microstructure of the anode support. From Figure 8, it can be observed that the electrochemical performance can be enhanced from 322.0 to 833.9 mW cm^{-2} and R_p/R_t can be reduced from 0.93 to 0.81 by adjusting their anode microstructures. It should be pointed out that the polarization resistance represents still over 80% of the total resistance and governs the overall cell resistance (Figure 8C), implying that electrochemical performances of the MT-SOFCs should be still mainly limited by the polarization resistance.[41] Therefore, the cell performances need to be further improved through optimizing the anode microstructure to decrease its polarization resistance.

4. CONCLUSIONS

The amount of the solid loading in the suspension is one of the key factors in controlling the microstructure of hollow fibers fabricated by the phase-inversion method. In this study, the correlation between the viscosity and the solid loading of the phase-inversion suspension was systematically investigated, and a critical point was found. A series of hollow fibers with different microstructures were successfully prepared using the phase-inversion approach, and the viscosity-related viscous fingering mechanism was adopted to explain the pore formation process, demonstrating that the hollow fiber with the desired microstructure could be tailored for specific applications by controlling the solid loading and the preparation method. Four representative NiO-YSZ hollow fibers were chosen as anode support to fabricate microtubular SOFCs. Electrochemical performances of the microtubular SOFCs with the configuration of Ni-YSZ/YSZ/YSZ-LSM have been tested at 750 °C with humidified H_2 as fuel and ambient air as oxidant, and maximum output power densities of 663.6, 833.9, 636.1, and 322.0 mW cm^{-2} were achieved, respectively, indicating that the cell performance can be enhanced via optimizing its anode microstructure.

AUTHOR INFORMATION

Corresponding Author

*E-mail: chenfa@cec.sc.edu. Phone: +1-803-777-4875. Fax: +1-803-777-0106.

Author Contributions

†These authors contributed equally to this work.

Notes

The authors declare no competing financial interest.

ACKNOWLEDGMENTS

The authors are grateful for the financial support from the U.S. National Science Foundation (DMR-1210792).

REFERENCES

(1) Singhal, S. C. Solid Oxide Fuel Cells for Stationary, Mobile, and Military Applications. *Solid State Ionics* **2002**, *152*, 405−410.

(2) Singhal, S. C.; Kendall, K., *High-temperature Solid Oxide Fuel Cells: Fundamentals, Design and Applications;* Elsevier: Oxford, U.K., 2003.

(3) Minh, N. Q. Ceramic Fuel Cells. *J. Am. Ceram. Soc.* **1993**, *76*, 563−588.

(4) Lawlor, V.; Griesser, S.; Buchinger, G.; Olabi, A.; Cordiner, S.; Meissner, D. Review of the Micro-tubular Solid Oxide Fuel Cell: Part I. Stack Design Issues and Research Activities. *J. Power Sources* **2009**, *193*, 387−399.

(5) Lawlor, V. Review of the Micro-tubular Solid Oxide Fuel Cell (Part II: Cell Design Issues and Research Activities). *J. Power Sources* **2013**, *240*, 421−441.

(6) Bujalski, W.; Dikwal, C. M.; Kendall, K. Cycling of Three Solid Oxide Fuel Cell Types. *J. Power Sources* **2007**, *171*, 96−100.

(7) Suzuki, T.; Hasan, Z.; Funahashi, Y.; Yamaguchi, T.; Fujishiro, Y.; Awano, M. Impact of Anode Microstructure on Solid Oxide Fuel Cells. *Science* **2009**, *325*, 852−855.

(8) Yang, C.; Li, W.; Zhang, S.; Bi, L.; Peng, R.; Chen, C.; Liu, W. Fabrication and Characterization of an Anode-supported Hollow Fiber SOFC. *J. Power Sources* **2009**, *187*, 90−92.

(9) Yang, C.; Jin, C.; Chen, F. Micro-tubular Solid Oxide Fuel Cells Fabricated by Phase-inversion Method. *Electrochem. Commun.* **2010**, *12*, 657−660.

(10) Zhao, F.; Jin, C.; Yang, C.; Wang, S.; Chen, F. Fabrication and Characterization of Anode-supported Micro-tubular Solid Oxide Fuel

Cell based on $BaZr_{0.1}Ce_{0.7}Y_{0.1}Yb_{0.1}O_{3-\delta}$ Electrolyte. *J. Power Sources* **2011**, *196*, 688−691.
(11) Othman, M. H. D.; Droushiotis, N.; Wu, Z.; Kelsall, G.; Li, K. High-Performance, Anode-Supported, Microtubular SOFC Prepared from Single-Step-Fabricated, Dual-Layer Hollow Fibers. *Adv. Mater.* **2011**, *23*, 2480−2483.
(12) Yang, C.; Ren, C.; Yu, L.; Jin, C. High Performance Intermediate Temperature Micro-tubular SOFCs with $Ba_{0.9}Co_{0.7}Fe_{0.2}Nb_{0.1}O_{3-\delta}$ as Cathode. *Int. J. Hydrogen Energy* **2013**, *38*, 15348−15353.
(13) Meng, X.; Gong, X.; Yin, Y.; Yang, N.; Tan, X.; Ma, Z.-F. Effect of the Co-spun Anode Functional Layer on the Performance of the Direct-methane Microtubular Solid Oxide Fuel Cells. *J. Power Sources* **2014**, *247*, 587−593.
(14) Alston, T.; Kendall, K.; Palin, M.; Prica, M.; Windibank, P. A 1000-cell SOFC Reactor for Domestic Cogeneration. *J. Power Sources* **1998**, *71*, 271−274.
(15) Wei, C. C.; Li, K. Yttria-stabilized Zirconia (YSZ)-based Hollow Fiber Solid Oxide Fuel Cells. *Ind. Eng. Chem. Res.* **2008**, *47*, 1506−1512.
(16) Yang, C. L.; Li, W.; Zhang, S. Q.; Liu, J. J.; Chen, C. S.; Liu, W. Fabrication and Evaluation of Electrolyte-Supported Hollow Fiber Solid Oxide Fuel Cells. *Adv. Mater. Res.* **2009**, *79*, 1691−1694.
(17) Liu, Y.; Hashimoto, S.-I.; Nishino, H.; Takei, K.; Mori, M.; Suzuki, T.; Funahashi, Y. Fabrication and Characterization of Micro-tubular Cathode-supported SOFC for Intermediate Temperature Operation. *J. Power Sources* **2007**, *174*, 95−102.
(18) Meng, X.; Gong, X.; Yang, N.; Tan, X.; Yin, Y.; Ma, Z.-F. Fabrication of Y_2O_3-stabilized-ZrO_2 (YSZ)/$La_{0.8}Sr_{0.2}MnO_{3-\alpha}$-YSZ Dual-Layer Hollow Fibers for the Cathode-supported Micro-tubular Solid Oxide Fuel Cells by a Co-spinning/co-sintering Technique. *J. Power Sources* **2013**, *237*, 277−284.
(19) Yamaguchi, T.; Shimizu, S.; Suzuki, T.; Fujishiro, Y.; Awano, M. Fabrication and Characterization of High Performance Cathode Supported Small-scale SOFC for Intermediate Temperature Operation. *Electrochem. Commun.* **2008**, *10*, 1381−1383.
(20) Yang, C.; Jin, C.; Chen, F. Performances of Micro-tubular Solid Oxide Cell with Novel Asymmetric Porous Hydrogen Electrode. *Electrochim. Acta* **2010**, *56*, 80−84.
(21) Loeb, S.; Sourirajan, S. Sea Water Demineralization by Means of an Osmotic Membrane. *Adv. Chem. Ser.* **1962**, *38*, 117.
(22) Fang, H.; Gao, J.; Wang, H.; Chen, C. Hydrophobic Porous Alumina Hollow Fiber for Water Desalination via Membrane Distillation Process. *J. Membr. Sci.* **2012**, *403*, 41−46.
(23) Han, M.-J. Effect of Propionic Acid in the Casting Solution on the Characteristics of Phase Inversion Polysulfone Membranes. *Desalination* **1999**, *121*, 31−39.
(24) Liu, T.; He, W.; Huang, H.; Wang, S.; Bouwmeester, H.; Chen, C.-S. $Ce_{0.8}Sm_{0.2}O_{1.9}$−$La_{0.8}Sr_{0.2}Cr_{0.5}Fe_{0.5}O_{3-\delta}$ Dual-Phase Hollow Fiber Membranes Operated under Different Gradients. *Ind. Eng. Chem. Res.* **2014**, *53*, 6131−6136.
(25) Liu, T.; Wang, Y.; Yuan, R.; Gao, J.; Chen, C.; Bouwmeester, H. J. Enhancing the Oxygen Permeation Rate of $Zr_{0.84}Y_{0.16}O_{1.92}$−$La_{0.8}Sr_{0.2}Cr_{0.5}Fe_{0.5}O_{3-\delta}$ Dual-Phase Hollow Fiber Membrane by Coating with $Ce_{0.8}Sm_{0.2}O_{1.9}$ Nanoparticles. *ACS Appl. Mater. Interfaces* **2013**, *5*, 9454−9460.
(26) Zydorczak, B.; Li, K.; Tan, X. Mixed Conducting Membranes—Macrostructure Related Oxygen Permeation Flux. *AlChE J.* **2010**, *56*, 3084−3090.
(27) Xu, G.; Yao, J.; Wang, K.; He, L.; Webley, P. A.; Chen, C.-s.; Wang, H. Preparation of ZIF-8 Membranes Supported on Ceramic Hollow Fibers from a Concentrated Synthesis Gel. *J. Membr. Sci.* **2011**, *385*, 187−193.
(28) Rezaei, F.; Lively, R. P.; Labreche, Y.; Chen, G.; Fan, Y.; Koros, W. J.; Jones, C. W. Aminosilane-Grafted Polymer/Silica Hollow Fiber Adsorbents for CO_2 Capture from Flue Gas. *ACS Appl. Mater. Interfaces* **2013**, *5*, 3921−3931.
(29) Mao, Y.; Li, J.; Cao, W.; Ying, Y.; Sun, L.; Peng, X. Pressure-assisted Synthesis of HKUST-1 Thin Film on Polymer Hollow Fiber at Room Temperature toward Gas Separation. *ACS Appl. Mater. Interfaces* **2014**, *6*, 4473−4479.
(30) Hilke, R.; Pradeep, N.; Madhavan, P.; Vainio, U.; Behzad, A. R.; Sougrat, R.; Nunes, S. P.; Peinemann, K.-V. Block Copolymer Hollow Fiber Membranes with Catalytic Activity and pH-Response. *ACS Appl. Mater. Interfaces* **2013**, *5*, 7001−7006.
(31) Lee, S.; Lee, J. S.; Lee, M.; Choi, J.-W.; Kim, S.; Lee, S. Separation of Sulfur Hexafluoride (SF_6) from Ternary Gas Mixtures using Commercial Polysulfone (PSf) Hollow Fiber Membranes. *J. Membr. Sci.* **2014**, *452*, 311−318.
(32) Strathmann, H.; Kock, K. The Formation Mechanism of Phase Inversion Membranes. *Desalination* **1977**, *21*, 241−255.
(33) Smolders, C.; Reuvers, A.; Boom, R.; Wienk, I. Microstructures in Phase-inversion Membranes. Part 1. Formation of Macrovoids. *J. Membr. Sci.* **1992**, *73*, 259−275.
(34) Boom, R.; Wienk, I.; Van den Boomgaard, T.; Smolders, C. Microstructures in Phase Inversion Membranes. Part 2. The Role of a Polymeric Additive. *J. Membr. Sci.* **1992**, *73*, 277−292.
(35) Wang, B.; Lai, Z. Finger-like Voids Induced by Viscous Fingering during Phase Inversion of Alumina/PES/NMP Suspensions. *J. Membr. Sci.* **2012**, *405*, 275−283.
(36) Othman, M. H. D.; Wu, Z.; Droushiotis, N.; Kelsall, G.; Li, K. Morphological Studies of Macrostructure of Ni−CGO Anode Hollow Fibres for Intermediate Temperature Solid Oxide Fuel Cells. *J. Membr. Sci.* **2010**, *360*, 410−417.
(37) Kingsbury, B. F.; Li, K. A Morphological Study of Ceramic Hollow Fibre Membranes. *J. Membr. Sci.* **2009**, *328*, 134−140.
(38) Kingsbury, B. F.; Wu, Z.; Li, K. A Morphological Study of Ceramic Hollow Fibre Membranes: a Perspective on Multifunctional Catalytic Membrane Reactors. *Catal. Today* **2010**, *156*, 306−315.
(39) Li, T.; Wu, Z.; Li, K. A Dual-structured Anode/Ni-mesh Current Collector Hollow Fibre for Micro-tubular Solid Oxide Fuel Cells (SOFCs). *J. Power Sources* **2014**, *251*, 145−151.
(40) Tyn, M. T.; Calus, W. F. Diffusion Coefficients in Dilute Binary Liquid Mixtures. *J. Chem. Eng. Data* **1975**, *20*, 106−109.
(41) Adler, S. B. Factors Governing Oxygen Reduction in Solid Oxide Fuel Cell Cathodes. *Chem. Rev.* **2004**, *104*, 4791−4844.
(42) Jacobson, A. J. Materials for Solid Oxide Fuel Cells. *Chem. Mater.* **2009**, *22*, 660−674.
(43) Chen, Y.; Bunch, J.; Li, T.; Mao, Z.; Chen, F. Novel Functionally Graded Acicular Electrode for Solid Oxide Cells Fabricated by the Freeze-tape-casting Process. *J. Power Sources* **2012**, *213*, 93−99.
(44) Jin, C.; Yang, C.; Chen, F. Effects on Microstructure of NiO−YSZ Anode Support Fabricated by Phase-inversion Method. *J. Membr. Sci.* **2010**, *363*, 250−255.
(45) Peng, S.; Zhou, D.; Wei, Y.; Li, Z.; Wang, H. A Novel U-shaped Anode-supported Hollow Fiber Solid Oxide Fuel Cell with Considerable Thermal Cycling Performance and Stability. *J. Membr. Sci.* **2012**, *417*, 80−86.
(46) Jin, C.; Liu, J.; Guo, W.; Zhang, Y. Electrochemical Characteristics of an $La_{0.6}Sr_{0.4}Co_{0.2}Fe_{0.8}O_3$-$La_{0.8}Sr_{0.2}MnO_3$ Multi-layer Composite Cathode for Intermediate-temperature Solid Oxide Fuel Cells. *J. Power Sources* **2008**, *183*, 506−511.